

Parasitic RF-SQUIDs in superconducting qubits due to wirebonds

B. Berlitz,¹ E. Daum,¹ S. Deck,² A.V. Ustinov,^{1,3} and J. Lisenfeld¹

¹*Physikalisches Institut, Karlsruhe Institute of Technology (KIT), Karlsruhe, Germany*

²*Lichttechnisches Institut (LTI), Karlsruhe Institute of Technology (KIT), Karlsruhe, Germany*

³*Institute for Quantum Materials, Karlsruhe Institute of Technology (KIT), Karlsruhe, Germany*

(Dated: 12 June 2025)

Superconducting qubits show great promise to realize practical quantum computers from micro-fabricated integrated circuits. However, their solid-state architecture bears the burden of parasitic modes in qubit materials and the control circuitry which cause decoherence and interfere with qubits. Here, we present evidence that wirebonds, which are used to contact the micro-circuits and to realize chip-to-chip airbridges, may contain parasitic Josephson junctions. In our experiment, such a junction was enclosed in a superconducting loop and so gave rise to the formation an RF-SQUID which interfered with a nearby flux-tunable transmon qubit. Periodic signatures observed in magnetic field sweeps revealed a strong AC-dispersive coupling of the parasitic RF-SQUID to both the qubit and its readout resonator, in addition to the DC-inductive coupling between RF-SQUID and qubit. Our finding sheds light on a previously unknown origin of decoherence due to parasitic Josephson junctions in superconducting circuits.

INTRODUCTION

Superconducting micro-circuits provide a tremendous test-bed to explore quantum coherence in electrically controlled solid-state systems. Different types of custom-tailored quantum two-state-systems (qubits) can be constructed from discrete eigenmodes of resonant circuits which combine the nonlinear inductance of Josephson tunnel junctions with capacitive and inductive elements^{1,2}. In recent years, this architecture has become a leading platform in the pursuit to realize large-scale quantum processors³. Yet, it remains a challenge to keep the macroscopic qubits well isolated from their environment and modes in the controlling circuitry which open channels for decoherence^{4,5}.

Qubits are typically operated in the microwave regime at resonance frequencies of a few GHz, and read out with weakly coupled and slightly detuned linear resonators that are accessed via on-chip transmission lines¹. Both readout resonators and transmission lines are typically made from coplanar waveguides, where a central signal line is placed between two ground planes.

To suppress unwanted slot-line modes, where the currents in the two ground planes oscillate out-of-phase, the state-of-the-art approach is to use micro-fabricated airbridges^{6–8} that shorten the ground planes at regular distances. However, in academic research environments and in prototyping experiments, the additional effort of lithographic airbridge fabrication is often spared. Instead, it is common practice to connect the ground plane sections at a few positions by manually placed airbridge wirebonds.

Here, we present evidence that parasitic Josephson junctions (p-JJs) may exist at flawed contacts between aluminum bonding wires and the natively oxidized aluminum film which is part of an on-chip ground

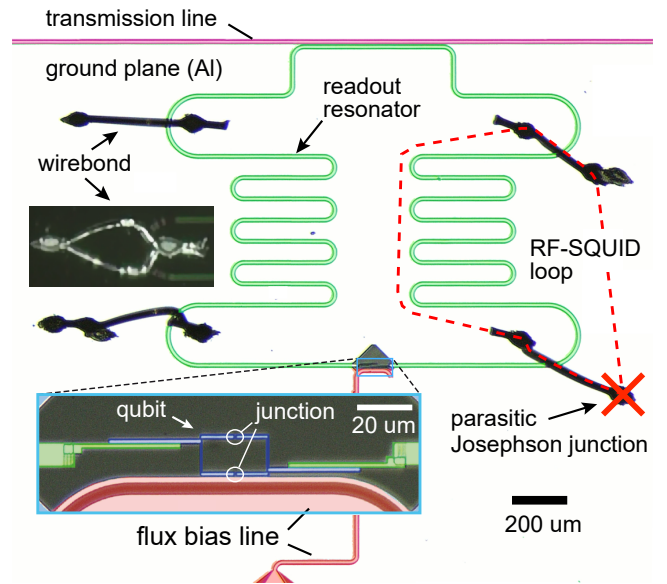


FIG. 1. False-colored sample micrograph showing the coplanar $\lambda/2$ readout resonator (green) that is coupled at both ends to a transmon qubit consisting of a DC-SQUID with two Josephson junctions (blue, see inset). Four wirebonds (black) connect the resonator's inner and outer ground planes to avoid slot-line modes. A parasitic Josephson junction within a wirebond (red cross) is enclosed in a superconducting loop (red dashed line) and so gives rise to an RF-SQUID that interferes with qubit and resonator.

plane or bond pad. This mechanism can give rise to a parasitic RF-SQUID (p-SQUID) that is formed by the p-JJ together with the inductances of involved wirebonds or lithographic connections which enclose the p-JJ in a superconducting loop. The quantized magnetic flux in the p-SQUID loop⁹ may then couple to

neighboring qubits if they are based on SQUIDs, such as flux qubits¹⁰ and fluxonium qubits¹¹, and if they employ DC-SQUIDs for tunability such as transmon qubits¹² and their couplers¹³. Moreover, AC-coupling of the p-SQUID's oscillatory eigenstates may induce dispersive shifts and avoided level crossings in neighboring qubits and resonators.

In our experiments, the existence of a p-SQUID was revealed from the characteristic signature it induces in the resonance frequency of a transmon qubit and its readout resonator during sweeps of the applied magnetic field. The data can well be fitted to a model that includes strong inductive and dispersive interactions of the p-SQUID with both the qubit and the readout resonator. The conclusion that a bond wire is involved in the creation of the p-SQUID is supported by measurements with applied in-plane and off-plane magnetic fields which reveal the three-dimensional form of the p-SQUID loop. This is strongly supported by the fact that removing the wirebonds from the sample also removed the p-SQUID signature. Our finding reveals that parasitic Josephson junctions in the wiring circuitry of superconducting qubits add further decoherence channels for superconducting qubits, and can even completely spoil their operability.

METHOD

Transmon qubits conventionally consist of one or two submicron-sized Josephson junctions that are shunted by a planar capacitor. In this work, we studied transmon qubits that employ larger-area Josephson junctions which possess sufficient self-capacitance so that no additional shunt capacitor is required. This so-called mergemon design^{14,15} significantly reduces the qubit footprint and promises less interference from charged two-level-system defects (TLS) known to reside at and near the interfaces of qubit electrodes^{16–19}. To enable in-situ tuning of the qubit's operation frequency, the junction is replaced by a DC-SQUID that can be flux-biased by a current in a nearby flux bias line. A photograph of the mergemon qubit sample is shown in the inset of Fig. 1.

The qubit's resonance frequency f_Q and state population are read out with a resonator that consists of a coplanar waveguide segment of electrical length $\lambda/2$, whose two open ends are each capacitively coupled to the opposing Mergemon electrodes as shown in Fig. 1. Since this design choice electrically isolates the inner ground plane of the coplanar resonator, we connected it by four airbridge wirebonds to the surrounding ground plane in order to suppress unwanted slot-line modes.

For small qubit-resonator coupling energies hg_{qr} and sufficiently large detuning $|\delta| = |(f_Q - f_r)| \gg g_{qr}$, the resonator's resonance frequency f_r obtains a dispersive

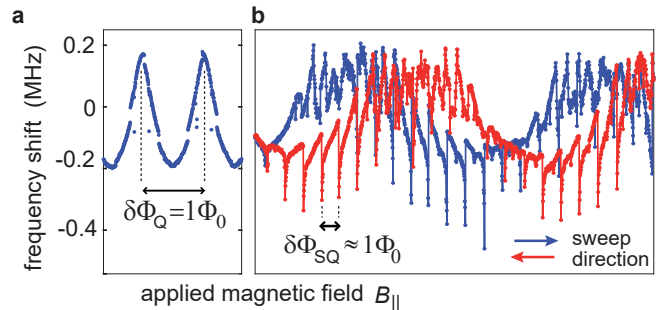


FIG. 2. Resonance frequency shift of the readout resonator vs. the applied in-plane magnetic field B_{\parallel} . **a** Sample without chip-to-chip wirebonds, showing the expected modulation as the qubit is tuned according to Eq. (2) via the induced flux Φ_Q in its DC-SQUID. A shift of 0 corresponds to $f_r = 4.5662$ GHz. **b** With the wirebonds still in place, a saw-tooth pattern and sharp dips in the resonator frequency were additionally observed at regular intervals. Sweeping the applied magnetic field in different directions (blue and red curves) inverts the asymmetry of this signature, and reveals a large hysteresis in the qubit frequency. A shift of 0 corresponds to $f_r = 4.1902$ GHz.

shift¹²

$$f'_r = f_r - \frac{g_{qr}^2}{\delta}. \quad (1)$$

The qubit transition frequency f_Q depends on the flux Φ_Q threading its DC-SQUID and can be approximated by¹²

$$hf_Q(\Phi_Q) = \sqrt{8E_c E_J(\Phi_Q)} - E_C, \quad (2)$$

where $E_C = e^2/2C_q$ is the charging energy of the qubit's capacitance C_q , e is the electron charge, $E_J = \hbar I_c/2e(\sqrt{\cos(\pi\Phi_Q/\Phi_0)^2 + d^2 \sin(\pi\Phi_Q/\Phi_0)^2})$ is the Josephson energy assuming two slightly different junctions with a total critical current I_c , $\Phi_0 = h/2e$ is the flux quantum, h is Planck's constant, and the junction's asymmetry factor $d = \frac{E_{J1} - E_{J2}}{E_{J1} + E_{J2}}$.

Using a network analyzer connected to the on-chip transmission line, the dispersive shift of the readout resonator is determined to estimate the qubit frequency as a function of the applied magnetic fields. In addition to the on-chip flux-bias line, the sample is enclosed in a solenoid to control the magnetic field B_{\parallel} in-plane of the qubit circuit, while another coil above the qubit chip applies a magnetic field B_{\perp} perpendicular to the chip's surface.

Figure 2a shows the expected periodic oscillations in the resonator's dispersive frequency shift when the qubit is tuned between its lowest and highest (at 4.125 GHz) resonance frequencies according to Eqs. (1) and (2) by sweeping the magnetic field B_{\parallel} . We note that B_{\parallel} should nominally be oriented perpendicular to the plane of the qubit's SQUID loop and therefore not couple to Φ_Q .

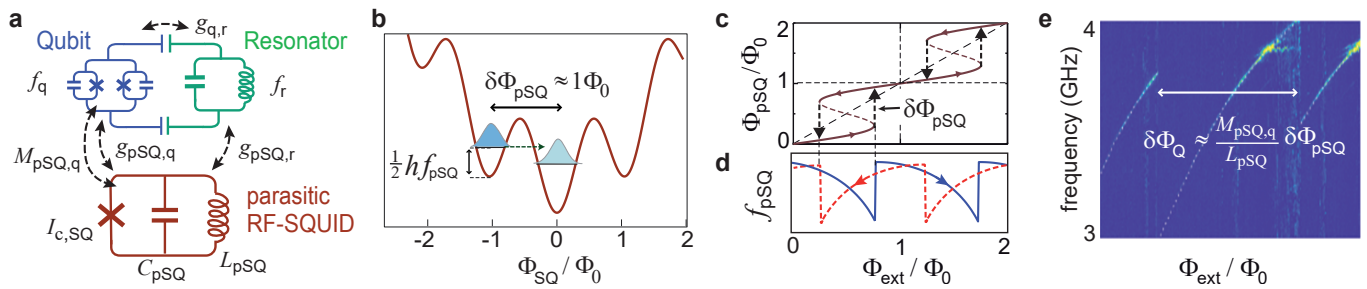


FIG. 3. **a** Circuit schematic including qubit, resonator, and the p-SQUID. Black symbols denote the model parameters. **b** Potential energy of an RF-SQUID as a function of the flux in its loop Φ_{pSQ} . Transitions between wells correspond to a change of Φ_{pSQ} by $\approx 1\Phi_0$. **c** RF-SQUID flux Φ_{pSQ} vs. the applied external flux Φ_{ext} for the different sweep directions (arrows). **d** RF-SQUID resonance frequency f_{pSQ} vs. Φ_{ext} . Dashed arrows indicate inter-well transitions. **e** The qubit resonance frequency f_Q (bright pixels), measured vs. the applied magnetic field $B_{||}$, shows a sawtooth behaviour due to the discretized flux induced from the p-SQUID.

Accordingly, we use these data to characterize the misalignment of the solenoid (see App. D for further details).

However, the data shown in Fig. 2a were acquired on the sample after the airbridge wirebonds had been removed. With the wirebonds still in place, the same experiment resulted in the data shown in Fig. 2b. Most prominently, the resonator frequency displayed a sawtooth-pattern and pronounced asymmetric dips at regular flux intervals in addition to the expected modulation. Moreover, there is a large hysteresis when the direction of the applied field is reversed, which also inverts the asymmetry of the signature.

RESULTS

In the following, we argue that these observations are explained by the presence of a parasitic RF-SQUID that is formed by a faulty airbridge wirebond that effectively contains a parasitic Josephson junction (p-JJ). We suspect that the p-JJ is contained in one of the four wirebonds that connect inner and outer ground planes of the resonator as shown in Fig. 1. The dashed red line in Fig. 1 indicates one of the possible superconducting loops that contribute to the p-SQUID's inductance together with that of other involved wirebonds and on-chip lithographic connections.

The schematic of the qubit circuit including the p-SQUID is shown in Fig. 3a, where C_{pSQ} is the capacitance of the readout resonator's inner ground plane plus the p-JJ's capacitance.

The potential energy of a large-inductance RF-SQUID is given by the sum of its inductive energy $E_L = \Phi_{pSQ}^2/2L_{SQ}$ and Josephson energy $E_{J,SQ}(\Phi_{pSQ}) \propto \cos(\Phi_{pSQ} - \Phi_{ext})$ as illustrated in Fig. 3b. The height of the potential barrier that localizes the ground state in one of the wells depends on the flux in the p-SQUID loop. Upon increasing the

bias flux Φ_{ext} , the potential barrier will decrease until the state may escape by quantum tunneling or thermal activation to the neighboring deeper well. This gives rise to the hysteretic function of Φ_{pSQ} vs. bias flux as illustrated in Fig. 3c.

The nonlinear and quantized flux in the p-SQUID loop Φ_{pSQ} couples via the mutual inductance $M_{q,sq}$ to the qubit flux Φ_Q . In magnetic field sweeps, the qubit frequency is thus modulated by a sawtooth-like pattern as it was also observed directly in spectroscopy, see Fig. 3e. This pattern is reproduced in the dispersive shift of the readout resonator frequency shown in Fig. 2b. The magnetic coupling between p-SQUID and the qubit also explains the hysteresis and inverted symmetry of the sawtooth pattern when the field sweep direction is reversed.

However, the p-SQUID's oscillatory eigenstates may also be AC-coupled to the qubit and resonator and induce dispersive resonance shifts and avoided level crossings via their respective (transversal) coupling strengths $g_{pSQ,q}$ and $g_{pSQ,r}$ as described by Eq. (1). The sharp dips observed in f_r (Fig. 2b) are explained by the dispersive coupling of the p-SQUID to qubit and resonator, which results in a large (quadratic) frequency shift according to Eq. (1) when the detuning becomes small. Figure 3d shows how the p-SQUID's plasma frequency f_{pSQ} decreases with the tunneling barrier until its state escapes to the next well. Since only dips but no avoided level crossings nor peaks were observed, the p-SQUID's resonance frequency must always be above that of the qubit and resonator. Because the dips remain visible when the qubit is tuned to its lowest frequency, where it is effectively decoupled from the resonator, there must be a strong direct dispersive coupling between the p-SQUID and the resonator, see App. B for details. This shows that parasitic RF-SQUIDs can have a strong impact on both qubits and resonators.

For a closer test of our model, we numerically simulate the data shown in Fig. 2b. For each value of bias

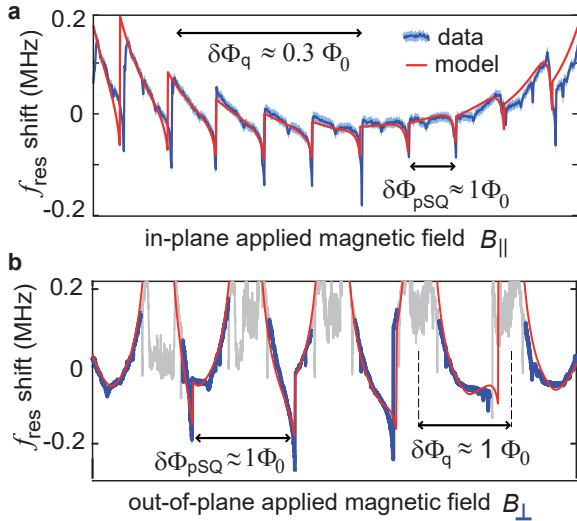


FIG. 4. Dispersive shift of the readout resonator (a) vs. applied in-plane magnetic field B_{\parallel} , and (b) vs. the applied perpendicular field B_{\perp} . The red lines show good agreement with the model's prediction, using the same fitting parameters for both measurements.

flux Φ_{ext} , the small oscillation frequency ω_{pSQ} in an initial well is found from the p-SQUID's potential energy²⁰ and the qubit resonance frequency ω_q is calculated from Eq. (2), taking into account that the flux in the qubit loop Φ_Q is a function of the applied field and the flux in the p-SQUID loop Φ_{pSQ} . The eigenfrequency of the resonator f_r is then obtained by solving the stationary Schrödinger equation for the circuit shown in Fig. 3a and its Hamiltonian

$$\frac{\hat{H}(\phi_x)}{h} = \begin{bmatrix} f_{r,0} & g_{r,q} & g_{\text{pSQ},r} \\ g_{q,r} & f_{q,0} & g_{\text{pSQ},q} \\ g_{\text{pSQ},r} & g_{\text{pSQ},q} & f_{\text{pSQ},0} \end{bmatrix}, \quad (3)$$

which contains the transversal coupling strengths between resonator, qubit, and p-SQUID as off-diagonal elements. The escape from the current potential well is implemented by initializing the p-SQUID's ground state in the next deeper well once the tunnel rate²¹ exceeds a value of $(20\text{s})^{-1}$ which corresponds to the time required for one measurement of f_r .

Figure 4 a shows a striking agreement between the model and the data. To test the hypothesis that a wirebond is involved in the loop of the p-SQUID, the experiment is repeated by sweeping the out-of-plane component of the applied magnetic field B_{\perp} as shown in Fig. 4b. A comparison of the flux periodicity of the p-SQUID (given by the distance between dips in f_r) with that of the qubit (the distance between the broader maxima in f_r) shows that the relative coupling of qubit and p-SQUID to the B-field depends on its direction. This is consistent with the three-dimensional geometry of the wirebond's loops (see App. D for details).

The model agrees excellently with both experiments for the same set of fit parameters (red lines in Figs. 4a and b). We note that the data obtained near maxima of the qubit frequency is distorted due to the small detuning of qubit and resonator, and has therefore been omitted from the fits. Since the least-squares fit involved 8 free parameters (see App. A), large uncertainties in the fitting values don't allow us to obtain detailed information on the origin of the parasitic junction that gave rise to the p-SQUID. However, the observed hysteresis clearly reveals the p-SQUID's multi-well potential associated with⁹ $\beta_{L,\text{pSQ}} = 2\pi L_{\text{pSQ}} \cdot I_{c,\text{pSQ}}/\Phi_0 > 1$. This places the p-SQUID in the parameter regime of flux-biased phase qubits²²⁻²⁴. Estimating the p-SQUID's inductance to $L_{\text{pSQ}} \approx 0.5\text{ nH}$ (see App. C), this corresponds to a critical current of the parasitic junction of $I_{c,\text{pSQ}} \gtrsim 1\mu\text{A}$. Aiming to identify the flawed bond after the sample was warmed up, the bond wire bridges were touched and heavily bent using the micro-manipulator of a bonding station. However, all bonds appeared stable and did not disconnect easily. We note that it has been proposed to utilize the discreteness of RF-SQUID flux states to provide a stable flux-bias source for qubits^{25,26}.

DISCUSSION

While it has been known that stray Josephson junctions between thin-film qubit electrodes are a source of qubit decoherence^{17,27}, our finding sheds light on related issues in the remaining circuitry and packaging. In our experiment, two out of four qubits on the chip were inoperable due to their strong interference with the parasitic RF-SQUID formed by a faulty chip-to-chip wirebond. Related issues may arise for instance from detrimental modes in flux bias lines that were terminated by a junction in a flawed wirebond. Problems with parasitic junctions due to flawed airbridges, bond wires, or bump-pads in flip-chip architectures²⁸, may rise in importance as quantum processors increase in size and complexity. The observed strong DC-magnetic and AC-electric interactions of parasitic RFSQUIDs can furthermore spoil the functionality of various other superconducting devices²⁹ such as for instance parametric amplifiers^{30,31}, RSFQ-logic³², MKID photon detectors³³, and passive resonator-based microwave filters³⁴.

ACKNOWLEDGMENTS

We acknowledge the contributions of Alexander Bilmes to the experimental setup and qubit fabrication. We thank Hannes Rotzinger for fruitful discussions and assistance in the laboratory. BB acknowledges help of Konstantin Händel with sample fabrication. This work was funded by Google, which we gratefully acknowledge.

Appendix A: Fit to the model

To compare the data shown in Figs. 4 to the system of interacting qubit, resonator, and p-SQUID, we simulate magnetic field sweeps and obtain the eigenfrequency of the resonator by numerical diagonalization of the Hamiltonian Eq. (3) as described in the main text. Best-fitting model parameters are then obtained by a least-square fit routine. These are listed in Table I and were used to plot the red lines in Fig. 4.

However, due to the large number and not fully independent model parameters, the confidence interval of most fitting parameters greatly exceeds their values so that we cannot obtain precise information on the p-SQUID's parameters and geometry. This could be improved with the help of finite element simulations of the p-SQUID's inductance and capacitance.

parameter	value	description
$f_{\text{res},0}$	4.19 GHz	uncoupled resonator frequency
$g_{\text{pSQ},r}$	10.2 MHz	coupling strength pSQUID-resonator
$g_{\text{pSQ},q}$	340 MHz	coupling strength pSQUID-qubit
ϕ_{slope}^Q	0.19 Φ_0	Φ_Q induced between well jumps
ϕ_{jump}^Q	0.12 Φ_0	Φ_Q jump at well jump
L_{pSQ}	1.23 nH	p-SQUID inductance
C_{pSQ}	3.1 pF	p-SQUID capacitance
$I_{c,\text{pSQ}}$	1.53 μA	p-SQUID critical current

TABLE I. Model parameters and their values that best fit the data as shown in Fig. 4. We note that due to large uncertainties in the fitting values, the fit only serves for a qualitative comparison with the model.

The parameters of the qubit and its coupling to the resonator (see Table II) were obtained from a fit to spectroscopy data on the sample after the wirebonds had been removed. We note that the readout resonator's frequency was 4.5662 GHz when the wirebonds were removed, and 4.1902 GHz with installed airbridge wirebonds as shown in Fig. 1.

parameter	value	description
E_J	12.3 GHz	qubit Josephson energy
$f_{q,\text{max}}$	4.125 GHz	maximum qubit frequency at zero flux
E_C	0.19 GHz	qubit charge energy
d	0.12	qubit JJ asymmetry factor
$g_{q,r}$	0.014 GHz	coupling strength qubit-resonator

TABLE II. Qubit parameters, obtained in spectroscopy after removal of wirebonds.

Appendix B: p-SQUID coupling to qubit and resonator

To illustrate our conclusion that the p-SQUID directly couples to the qubit's readout resonator, we set different

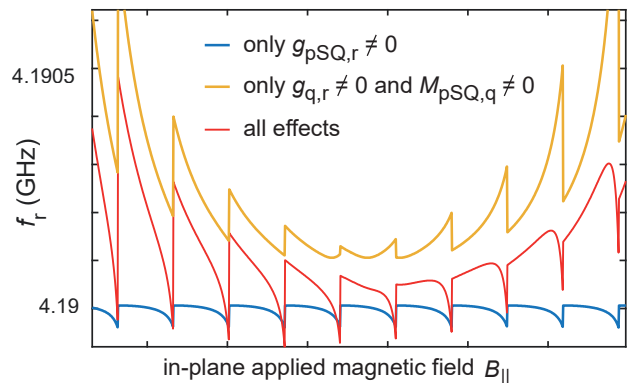


FIG. 5. Resonator resonance frequency f_r vs. B_{\parallel} obtained from the Hamiltonian Eq. 3 when different coupling parameters are set to zero. Without a direct transversal coupling between p-SQUID and the resonator (yellow line), the sharp dips near the minimum of f_r are absent. The blue line shows only the dips induced by this direct interaction when both the magnetic coupling $M_{\text{pSQ},q}$ and AC coupling $g_{\text{SQ},q}$ between qubit and p-SQUID are set to zero.

parameters in the Hamiltonian Eq. (3) to zero and compare the model's prediction shown in Fig. 5. This shows that the sharp dips in f_r are caused by the dispersive shift on f_r due to nonzero p-SQUID-resonator transversal coupling $g_{\text{pSQ},r}$.

Appendix C: Bond wire inductance

Superconducting bond wires are typically made from aluminum wires of 20 to 25 μm diameter. A common rule-of-thumb is that 1mm of bond wire has an inductance of 1 nH. We compare this rule with the textbook formula³⁵

$$L = \frac{\mu_0}{2\pi} l \left(\log \left(\frac{2l}{r} \right) - 1 \right) \quad (\text{C1})$$

where l is the wire length and r the wire radius as shown in Figure 6 b. Measuring the lengths of the bond wires on our sample using optical microscopy from different angles (see Fig. 6a), we estimate their inductances to range from 240pH to 380 pH.

Appendix D: Field alignment and p-SQUID geometry

To estimate the misalignment of the in-plane magnetic field with respect to the chip's ground plane, we measure the periodicity of the qubit resonance frequency as a function of B_{\parallel} . Using the area of the qubit's DC-SQUID loop $A = 276 \mu\text{m}^2$, we calculate the misalignment angle α from the relation

$$\alpha = \sin^{-1} \left(\frac{\Phi_0}{AB_{\parallel}} \right) = 0.0725^\circ, \quad (\text{D1})$$

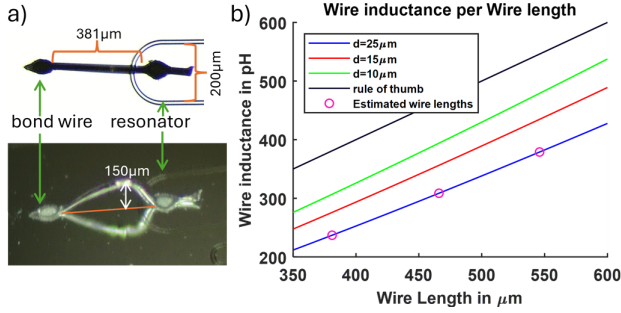


FIG. 6. a) Optical micrographs of bonding wires. By comparing micrographs from different angles, the lengths of the bonding wires were measured to be 466, 381, 546 and 466 μm . b) The bond wire inductance per length of wire calculated by the textbook formula for different wire diameters (blue, red and green line).

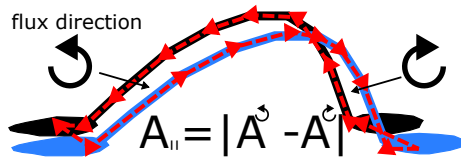


FIG. 7. Illustration of adjacent wirebond loops from an in-plane perspective. Their effective loop size A is the difference of the area enclosed by loop segments of opposite current directions.

where the field $B_{||}$ generated by the solenoid is estimated from COMSOL simulations.

The p-SQUID's effective loop area $A_{pSQ,||}$ can accordingly be estimated from the periodicity of the dips in the resonator frequency (Fig. 4) as a function of the estimated $B_{||}$ -field strength. This results in

$$A_{pSQ,||} = \frac{\Phi_0}{B_{||}^0} = 2068 \mu\text{m}^2. \quad (\text{D2})$$

The effective p-SQUID area is rather small due to gradiometer effects in the four parallel wirebond connections, see Fig. 1 and Fig. 7.

BIBLIOGRAPHY

- ¹I. Siddiqi, "Engineering high-coherence superconducting qubits," *Nature Reviews Materials* **6**, 875–891 (2021).
- ²A. Krasnok, P. Dhakal, A. Fedorov, P. Frigola, M. Kelly, and S. Kutsaev, "Superconducting microwave cavities and qubits for quantum information systems," *Applied Physics Reviews* **11** (2024).
- ³M. Kjaergaard, M. E. Schwartz, J. Braumüller, P. Krantz, J. I.-J. Wang, S. Gustavsson, and W. D. Oliver, "Superconducting qubits: Current state of play," *Annual Review of Condensed Matter Physics* **11**, 369–395 (2020).
- ⁴C. Müller, J. H. Cole, and J. Lisenfeld, "Towards understanding two-level-systems in amorphous solids: insights from quantum circuits," *Reports on Progress in Physics* **82**, 124501 (2019).

- ⁵S. Huang, B. Lienhard, G. Calusine, A. Vepsäläinen, J. Braumüller, D. K. Kim, A. J. Melville, B. M. Niedzielski, J. L. Yoder, B. Kannan, *et al.*, "Microwave package design for superconducting quantum processors," *PRX Quantum* **2**, 020306 (2021).
- ⁶M. Abuwasib, P. Krantz, and P. Delsing, "Fabrication of large dimension aluminum air-bridges for superconducting quantum circuits," *Journal of Vacuum Science & Technology B* **31** (2013).
- ⁷Z. Chen, A. Megrant, J. Kelly, R. Barends, J. Bochmann, Y. Chen, B. Chiaro, A. Dunsworth, E. Jeffrey, J. Mutus, *et al.*, "Fabrication and characterization of aluminum airbridges for superconducting microwave circuits," *Applied Physics Letters* **104** (2014).
- ⁸A. Dunsworth, R. Barends, Y. Chen, Z. Chen, B. Chiaro, A. Fowler, B. Foxen, E. Jeffrey, J. Kelly, P. Klimov, *et al.*, "A method for building low loss multi-layer wiring for superconducting microwave devices," *Applied Physics Letters* **112** (2018).
- ⁹J. Clarke and A. I. Braginski, *The SQUID handbook. Vol. 2. Applications of SQUIDS and SQUID systems* (Wiley-VCH, 2006).
- ¹⁰I. Chiorescu, Y. Nakamura, C. M. Harmans, and J. Mooij, "Coherent quantum dynamics of a superconducting flux qubit," *Science* **299**, 1869–1871 (2003).
- ¹¹V. E. Manucharyan, J. Koch, L. I. Glazman, and M. H. Devoret, "Fluxonium: Single cooper-pair circuit free of charge offsets," *Science* **326**, 113–116 (2009).
- ¹²J. Koch, M. Y. Terri, J. Gambetta, A. A. Houck, D. Schuster, J. Majer, A. Blais, M. H. Devoret, S. M. Girvin, and R. J. Schoelkopf, "Charge-insensitive qubit design derived from the cooper pair box," *Physical Review A* **76**, 042319 (2007).
- ¹³Y. Chen, C. Neill, P. Roushan, N. Leung, M. Fang, R. Barends, J. Kelly, B. Campbell, Z. Chen, B. Chiaro, *et al.*, "Qubit architecture with high coherence and fast tunable coupling," *Physical review letters* **113**, 220502 (2014).
- ¹⁴R. Zhao, S. Park, T. Zhao, M. Bal, C. McRae, J. Long, and D. Pappas, "Merged-element transmon," *Physical Review Applied* **14**, 064006 (2020).
- ¹⁵H. Mamin, E. Huang, S. Carnevale, C. T. Rettner, N. Arellano, M. Sherwood, C. Kurter, B. Trimm, M. Sandberg, R. M. Shelby, *et al.*, "Merged-element transmons: Design and qubit performance," *Physical Review Applied* **16**, 024023 (2021).
- ¹⁶C. Wang, C. Axline, Y. Y. Gao, T. Brecht, Y. Chu, L. Frunzio, M. Devoret, and R. J. Schoelkopf, "Surface participation and dielectric loss in superconducting qubits," *Applied Physics Letters* **107**, 162601 (2015).
- ¹⁷J. Lisenfeld, A. Bilmes, A. Megrant, R. Barends, J. Kelly, P. Klimov, G. Weiss, J. M. Martinis, and A. V. Ustinov, "Electric field spectroscopy of material defects in transmon qubits," *npj Quantum Information* **5**, 1–6 (2019).
- ¹⁸A. Bilmes, A. Megrant, P. Klimov, G. Weiss, J. M. Martinis, A. V. Ustinov, and J. Lisenfeld, "Resolving the positions of defects in superconducting quantum bits," *Scientific Reports* **10**, 1–6 (2020).
- ¹⁹C. E. Murray, "Material matters in superconducting qubits," *arXiv preprint arXiv:2106.05919* (2021).
- ²⁰D. J. Van Harlingen, T. L. Robertson, B. L. T. Plourde, P. A. Reichardt, T. A. Crane, and J. Clarke, "Decoherence in josephson-junction qubits due to critical-current fluctuations," *Phys. Rev. B* **70**, 064517 (2004).
- ²¹K. Likharev, "Macroscopic quantum tunneling and dissipation in josephson junctions and squids," *Physica B+C* **108**, 1079–1080 (1981).
- ²²K. Lang, S. Nam, J. Aumentado, C. Urbina, and J. M. Martinis, "Banishing quasiparticles from josephson-junction qubits: Why and how to do it," *IEEE Transactions on Applied Superconductivity* **13**, 989–993 (2003).
- ²³J. M. Martinis, "Superconducting phase qubits," *Quantum information processing* **8**, 81–103 (2009).
- ²⁴J. Lisenfeld, *Experiments on superconducting Josephson phase quantum bits* (Citeseer, 2008).

- ²⁵M. G. Castellano, F. Chiarello, G. Torrioli, and P. Carelli, “Static flux bias of a flux qubit using persistent current trapping,” *Superconductor Science and Technology* **19**, 1158 (2006).
- ²⁶L. Jiang, Y. Xu, S. Li, Z. Yan, M. Gong, T. Rong, C. Sun, T. Sun, T. Jiang, H. Deng, *et al.*, “In situ qubit frequency tuning circuit for scalable superconducting quantum computing: Scheme and experiment,” arXiv preprint arXiv:2407.21415 (2024).
- ²⁷A. Dunsworth, A. Megrant, C. Quintana, Z. Chen, R. Barends, B. Burkett, B. Foxen, Y. Chen, B. Chiaro, A. Fowler, *et al.*, “Characterization and reduction of capacitive loss induced by sub-micron josephson junction fabrication in superconducting qubits,” *Applied Physics Letters* **111**, 022601 (2017).
- ²⁸D. Rosenberg, D. Kim, R. Das, D. Yost, S. Gustavsson, D. Hover, P. Krantz, A. Melville, L. Racz, G. Samach, *et al.*, “3d integrated superconducting qubits,” *npj quantum information* **3**, 42 (2017).
- ²⁹A. I. Braginski, “Superconductor electronics: Status and outlook,” *Journal of superconductivity and novel magnetism* **32**, 23–44 (2019).
- ³⁰C. Macklin, K. O’Brien, D. Hover, M. Schwartz, V. Bolkhovskiy, X. Zhang, W. Oliver, and I. Siddiqi, “A near-quantum-limited josephson traveling-wave parametric amplifier,” *Science* **350**, 307–310 (2015).
- ³¹J. Aumentado, “Superconducting parametric amplifiers: The state of the art in josephson parametric amplifiers,” *IEEE Microwave magazine* **21**, 45–59 (2020).
- ³²P. Bunyk, K. Likharev, and D. Zinoviev, “Rsfq technology: Physics and devices,” *International journal of high speed electronics and systems* **11**, 257–305 (2001).
- ³³B. A. Mazin, “Microwave kinetic inductance detectors: The first decade,” in *AIP Conference Proceedings*, Vol. 1185 (American Institute of Physics, 2009) pp. 135–142.
- ³⁴D. E. Oates, “Microwave resonators and filters,” in *Handbook of Superconductivity* (CRC Press, 2022) pp. 596–608.
- ³⁵E. B. Rosa, “The self and mutual inductances of linear conductors,” *Bulletin of the Bureau of Standards* **4**, 301–344 (1908), scientific Paper No. 80.